PHYSICAL REVIEW B **87**, 104504 (2013)

Athermal energy loss from x-rays deposited in thin superconducting films on solid substrates

Alexander G. Kozorezov,[1] Colin J. Lambert,[1] Simon R. Bandler,[2] Manuel A. Balvin,[2] Sarah E. Busch,[2] Peter N. Nagler,[2,3] Jan-Patrick Porst,[2,3] Stephen J. Smith,[2] Thomas R. Stevenson,[2] and John E. Sadleir[2]

[1]*Department of Physics, Lancaster University, Lancaster, United Kingdom*
[2]*NASA/Goddard Space Flight Center, Greenbelt, Maryland 20771, USA*
[3]*Physics Department, Brown University, Providence, Rhode Island 02912, USA*

(Received 12 December 2012; revised manuscript received 5 February 2013; published 5 March 2013)

When energy is deposited in a thin-film cryogenic detector, such as from the absorption of an x-ray, an important feature that determines the energy resolution is the amount of athermal energy that can be lost to the heat bath prior to the elementary excitation systems coming into thermal equilibrium. This form of energy loss will be position dependent and therefore can limit the detector energy resolution. An understanding of the physical processes that occur when elementary excitations are generated in metal films on dielectric substrates is important for the design and optimization of a number of different types of low-temperature detectors. We have measured the total energy loss in one relatively simple geometry that allows us to study these processes and compare measurements with calculation based upon a model for the various different processes. We have modeled the athermal phonon energy loss in this device by finding an evolving phonon distribution function that solves the system of kinetic equations for the interacting system of electrons and phonons. Using measurements of device parameters such as the Debye energy and the thermal diffusivity we have calculated the expected energy loss from this detector geometry, and also the position-dependent variation of this loss. We have also calculated the predicted impact on measured spectral lineshapes and have shown that they agree well with measurements. In addition, we have tested this model by using it to predict the performance of a number of other types of detector with different geometries, where good agreement is also found.

DOI: 10.1103/PhysRevB.87.104504 PACS number(s): 74.25.Ld, 74.25.Kc, 74.25.F−

I. INTRODUCTION

An understanding of the key processes that take place when energy is deposited is important for any type of radiation detector. In this paper we present direct measurements and detailed calculations of energy loss and fluctuations in this loss from athermal phonons that escape from a metal film into a dielectric substrate. This loss mechanism can influence the measured energy resolution performance of a wide variety of particle detectors.

There are two major classes of low-temperature photon detectors. The first is a class of devices operating under nonequilibrium conditions; the best examples of these are superconducting tunnel junctions (STJs) and microwave kinetic inductance detectors (MKIDs). For these detectors, nonequilibrium quasiparticles are created in the process of energy down conversion, which results in the breaking of numerous Cooper pairs. This down-conversion process typically lasts from several tens to hundreds of picoseconds. During the down-conversion process the photon energy is transformed into electronic excitations and phonons, the properties of nonequilibrium distribution of quasiparticles and phonons being used to determine the energy deposited. The mechanisms for determining the energy partition between the two systems far away from equilibrium are important and lead to the well-known statistical Fano limit for the resolution of this type of detector.

A second class of low-temperature detectors are equilibrium devices. These include microcalorimeters and bolometers that are used to measure the energy of single photons and the power from a flux of photons, respectively. In these devices the different types of excitations rapidly come into thermal quasi-equilibrium at a temperature slightly above that of the thermal bath. We consider the distributions to have reached quasithermal equilibrium when the electron and phonon systems are in equilibrium with each other, but the temperature of these systems is still changing. The measured signal is determined from the mean energy of all excitations and is determined by the temperature excursion. In low temperature ($\leqslant$1 K) microcalorimeters thermal quasi-equilibrium is typically established on the time scale of less than 1 μs, and Fano fluctuations are completely washed out.

One key question that is relevant to all types of detectors is whether the whole deposited energy is retained in the sensing element and converted into the response signal. Energy that is leaked from the sensor prior to generating the ultimate number of quasiparticles or establishing thermal quasi-equilibrium may naturally occur in all types of detectors. Although the energy down-conversion process is usually fast, a significant fraction of the photon energy can be accumulated within the energetic phonon system (athermal phonons). Depending upon the geometry of the detector, these phonons have some probability of escape from metal films into a dielectric support, such as a silicon wafer. This can result in a significant deficit in the energy detected. A number of different detector types have athermal phonons produced in films fabricated on solid substrates, where athermal phonon escape can degrade performance either from the deficit in the amount of energy finally detected, or through variations in the amount of energy lost, depending upon the location of the initial photon interaction. An example of performance being affected by the deficit in energy is in single-photon detectors operating at visible and near-infrared wavelengths.[1] Here the spectral resolving power is typically not very high ($\sim$10), and therefore variations in energy loss $\sim$1% are not important. But the loss in energy, as high as 50% in these low-energy photon detectors,

can significantly affect the performance. An example where the broadening of energy resolution is more important than the energy deficit is in some x-ray detectors fabricated on solid substrates with STJ sensors. Variation in athermal phonon escape was identified as the mechanism responsible for these devices not being able to achieve Fano-limited spectral resolution in the optical and soft-x-ray band.[2–4]

Traditional x-ray microcalorimeter geometries often employ thin-film membranes[5] or narrow silicon legs[6] to isolate the temperature sensor from the substrate. In these geometries athermal phonon energy loss is often substantially reduced or almost eliminated. With a membrane geometry, athermal phonons are preferentially thermalized or reabsorbed rather than lost from the detector due to the physical geometry. An energy resolving power of over 3000 has been achieved while detecting 6 keV photons,[7] and over 4000 while detecting 100 keV photons.[8] While this very high spectroscopic performance is achievable with this type of device geometry, the low thermal conductance of the membranes can lead to detectors that return to the temperature of the thermal bath with a relatively slow time constant, leading to lower count-rate capability than desired. There are many applications where high count-rate capability and high spectral resolution is desired.[9] Another drawback to using membrane supports is that large arrays of fine-pitch and close-packed pixels become more difficult to design and fabricate.

To produce a fast microcalorimeter that does not have degraded energy resolution, a geometry was fabricated with a transition-edge sensor (TES) on a solid substrate which is attached to an x-ray absorber supported by attachments points ("stems") that supports it above the sensor and substrate. By making these contact points small, the effects of athermal energy loss were minimized.[10] It was found that, for this geometry, the energy resolution degraded as the area of contact of the "stem contact" increased. The detector geometry with the smallest contact area between absorber and solid substrate was not only fast, but also demonstrated the best energy resolution seen by any low-temperature detector at 6 keV of 1.6 eV full width at half maximum (FWHM).[10] In similar devices where the absorber was twice as thick, the dependence of energy resolution on contact area was not apparent. Thus there was strong evidence for the energy resolution of this type of detector being highly dependent on the amount of athermal phonon loss, which is very geometry dependent. It is the understanding of the important physical processes that takes place when athermal phonons are generated in metal films that motivates this work. With this understanding, it will be possible to predict the effects on performance for a wide variety of absorber and stem dimensions. It will also be possible to optimize the geometry and material properties according to the requirements of the different detector types, taking into account the need to simplify fabrication processes as much possible.

In Sec. II we describe two experimental results that are affected by athermal phonon loss. In the first, we consider the performance for when x-rays are stopped in a microcalorimeter sensor film on a solid substrate without an absorber. In this type of geometry, the performance is known to be poor for decades due to athermal phonon loss. However, we use the width and shape of the spectral response from the almost monoenergetic source as an important measurement for comparison with our model. In the second, we look at signals from a microcalorimeter with a similar film on a solid substrate with an absorber attached. In this latter case, by comparing the signal profiles when x-rays are stopped in the absorber with those that are stopped in the sensor, we are able to measure important parameters in the energy-transport process. For both of these experiments the sensor is a magnetic penetration-depth thermometer (MPT),[11] a relatively new type of thin-film thermometer. It is particularly useful for these studies because of important sensor properties that we describe in Sec. II that ensure that the energy loss observed is dominated by the processes modeled. In Secs. III–V we describe a framework for studying how athermal phonon loss can affect the performance and characterization of different detector designs on solid substrates.

Prior to this paper there have been no direct measurements or calculations of energy loss and fluctuations in this loss that will influence measured spectral lineshapes. For the high resolving power of TES sensors fabricated on suspended membranes this was not important. For STJs the energy loss can only be evaluated indirectly through line shifts which must be correlated with certain sharp features in the dependence of the photon absorption coefficient on energy either due to peaks associated with the onset of interband transitions for the optical photon range or in x-ray absorption-edge spectroscopy for soft x-rays. In both cases the abrupt change in photon absorption coefficient and distribution of absorption sites result in strong variations in energy loss and corresponding line shifts. However, indirect measurements cannot yield sufficiently accurate results because of practical experimental details such as the poor quantum efficiency of thin metal films and often-complicated fine x-ray absorption spectra. The direct measurements of energy loss from thin-layer systems through athermal phonons therefore is of great importance. The results are relevant to a wide variety of thin-film metallic sensor geometries, where the sensors can be transition-edge sensors (TESs),[12] metallic magnetic calorimeters (MMC),[13] magnetic penetration thermometers,[11] MKIDs, STJs, and nanobolometers.

II. EXPERIMENTAL DETAILS

In this section we describe two experimental results that provide information about the energy loss that occurs when an x-ray is stopped in a thin metallic film on a solid dielectric substrate, prior to the film reaching quasithermal equilibrium. For both of these experiments, the quasithermal signal is measured using a magnetic penetration thermometer (MPT).[11,14,15] This type of thermometer utilizes the temperature-dependent diamagnetic susceptibility of a superconducting film. A schematic diagram of the two experiments is depicted in Fig. 1, which shows the layout of a MPT-based x-ray microcalorimeter. When an x-ray is stopped in the gold absorber the entire absorber and the MPT superconducting film quickly come into thermal equilibrium. The MPT film is a bilayer consisting of molybdenum and gold. The temperature of the microcalorimeter ideally rises according to

$$\Delta T = \Delta E / C_{\text{total}}, \tag{1}$$

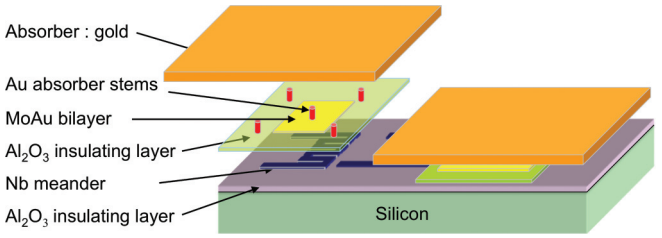

FIG. 1. (Color online) Schematic depicting the components of a MPT microcalorimeter (left) and an assembled pixel (right).

where ΔE is the energy of the x-ray, and C_{total} is the heat capacity of the absorber plus the MPT bilayer. The temporal profile of a typical event where an x-ray is stopped in the absorber is shown in the inset of Fig. 2. After the first $\sim 1\ \mu$s the electron and phonon systems are in equilibrium, but the temperature of this system is changing. Thus we consider the device to be in quasithermal equilibrium. After the temperature rises, the microcalorimeter decays back to the temperature of the heat bath with an exponential decay time constant given by C_{total}/G, where G is the thermal conductance of the MPT film to the substrate. G is determined by the Kapitza conductance of the MPT film to the dielectric substrate below. The signal is read out with a pickup coil that is beneath the MPT superconducting film. This pickup is connected to the input coil of a superconducting quantum interference device (SQUID) forming a purely superconducting loop. As the temperature rises, the MPT diamagnetic susceptibility is reduced, and the inductance of the pickup coil increases. The inductance $[L_p(T)]$ is sensed from current seen through the SQUID input (I_i) according to

$$I_i = \frac{-I_b[L_p(\infty) - L_p(T)]}{L_p(T) + L_i}, \tag{2}$$

where L_i is the sum of the SQUID input inductance and stray inductance, and I_b is the near-constant bias current supplied to the parallel combination of the SQUID input coil and the MPT pickup coil, provided by a large ballast inductor in the bias circuit. I_b is actually a persistent dc current that is applied

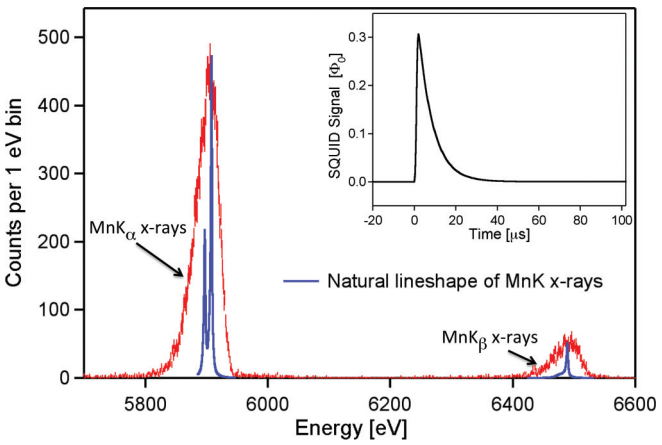

FIG. 2. (Color online) Spectrum from Mn K α x-rays deposited directly into MPT bilayer. The natural lineshape of the Mn K α x-rays is shown as the narrow solid lines underneath the data points. The inset shows the temporal profile of a typical Mn K α pulse.

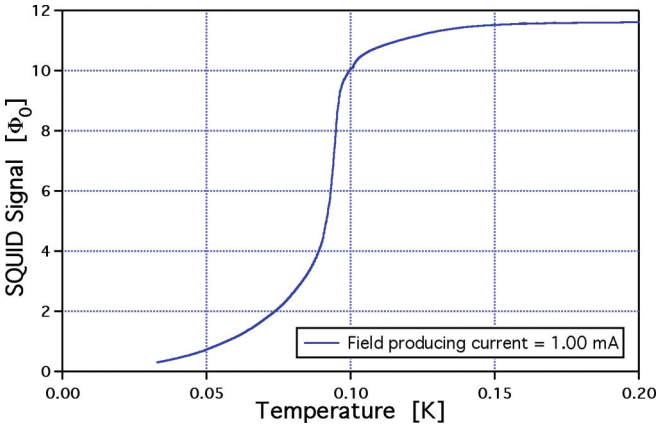

FIG. 3. (Color online) Measured SQUID signal as a function of temperature for MPT without absorber attached. $I_b = 1.0$ mA, producing an anisotropic magnetic field in the region of the MPT bilayer.

with a procedure that ensures that almost all of the current flows through the pickup coil.[16] The magnetic field produced by the pickup is nonisotropic and has been investigated in detail by Fleischmann *et al.*[13] In Fig. 3 we see an example of a SQUID signal as a function of temperature with an anisotropic field, which is approximately the temperature dependence of the MPT diamagnetic susceptibility. Unlike many other microcalorimeters, the MPT film has no electrical connections, so the possibility of electric connections that could allow energy loss through these contacts is eliminated.[17]

These MPT microcalorimeters are fabricated using standard microfabrication techniques.[18] There is a 250-nm-thick Al_2O_3 layer that provides isolation between the Si substrate and the first Nb layer, which forms the pickup coil. To isolate the MoAu sensor from the Nb pickup coil, we anodize the Nb, forming a 50-nm-thick Nb_2O_5 layer and then deposit a 250-nm-thick layer of Al_2O_3. A second Nb layer is then deposited to form low-inductance microstrip leads in all regions of the circuit except that of the pickup coil. Deposited over the area of the insulated pickup coil is the MoAu superconducting bilayer. The lower layer of the bilayer is 50-nm-thick Mo, and the upper layer is 330-nm-thick Au. In the first and second experiments the pickup coil had different geometries and calculated inductances of 0.76 and 0.53 nH, respectively. The MPT chip is connected to a separate SQUID chip with aluminum wirebonds, which contribute a stray inductance, typically measured to be $\approx$1.6 nH. Low-temperature characterization of our devices is performed in an adiabatic demagnetization refrigerator capable of reaching a minimum temperature of 30 mK. Our readout is accomplished using a two-stage SQUID provided by PTB-Berlin.[19] The first-stage SQUID has an input inductance of 1.8 nH, an input coupling of 5.4 $\mu A/\Phi_0$, and the overall readout has a broadband noise level that is less than 0.4 $\mu\Phi_0/\sqrt{\text{Hz}}$ at our operating temperature referred to the first-stage SQUID. The SQUIDs are read out using Magnicon SQUID electronics. Further details of our experimental procedure can be found in Rotzinger *et al.*[16]

In the first experiment, where there was no x-ray absorber, the x-rays were stopped directly in the MPT film. The main part

of the x-ray spectrum of pulse sizes is shown in Fig. 2. These signals are from 5.9 keV Mn K α x-rays that are produced when a radioactive ^{55}Fe source undergoes electron capture; signals from Mn K β were also observable at a lower count rate. The ratio of Mn K α and K β signal sizes, 500 eV apart, was used to calibrate the responsivity. The Mn K α x-rays are practically monoenergetic on the scale of the signal-size variation seen in this measurement. Based upon the signal and noise, the detector resolution for this measurement was 4.1 eV (FWHM) and the Mn K α complex extends only over a range of 10 eV, as seen in Fig. 2. We are able to compare the distribution of pulse sizes with those we would expect from mechanisms that we can model to learn about energy loss processes. Figure 3 shows the SQUID output as a function of temperature for this particular device. For this measurement with $I_b = 1.0$ mA, it was necessary to operate at a temperature of 115 mK. This ensured a responsivity that was only slightly nonlinear with a signal gain that could be accurately calibrated. It also ensured that the response from the x-ray signal was not too large to maintain the flux-locked loop of the SQUID readout from the $\sim$12 mK temperature rise that is seen on the time scale of the signal rise time which is $\sim$0.2 μs.

In the second experiment, with a different geometry MPT sensor coil, the x-ray absorber is attached and the majority of x-rays are stopped in this absorber. The absorber is a thin gold foil that is suspended above and coupled to the MoAu film; the absorber dimensions are $250 \times 250 \times 2.8$ μm^3. In Fig. 1 the connection points are shown schematically as solid stems; for these devices the contact stems were small regions where the absorber material is lowered to contact the sensor and substrate with small contact points that are 3.5 μm $\times$ 3.5 μm. There was a single contact point onto MoAu, and four contact points onto just the dielectric substrate that were introduced to add mechanical stability. The total area of contact of these stems is just 0.1% of the area of the MoAu. The superconducting transition temperature was lower for this experiment and the temperature of operation of 35 mK is at the steepest part of the MPT transition curve for $I_b = 0.38$ mA[14]. When x-rays are stopped in the absorber, i.e., when the whole energy of the x-ray was retained in the spectrometer following its absorption, the measured spectral resolution of Mn K α complex was 4.3 eV (FWHM).[14] This spectral resolution level is consistent with the resolution expected based upon the signal and noise. It is only limited by the microcalorimeter thermodynamic fluctuations and the SQUID amplifier noise level, given the temperature responsivity of this device under the operating conditions. Thus for this design, with a relatively small contact area between the absorber and solid substrate, the energy resolution is apparently not affected by the degrading effects of athermal phonon loss. In this respect it is close to "ideal."

A small fraction of the x-rays passed through the absorber and were stopped in the MPT film. Based upon the geometry of the device and the known attenuation lengths of the different materials we estimate that 1.55% of the 5.9 keV x-rays incident on the absorber actually pass through it and are stopped in the Mo/Au sensor. The measured fraction of 1.85% $\pm$ 0.23% is within the range of what we would expect given the known accuracy of absorber thickness ($\sim$10%). The events where the x-rays are stopped in the bilayer have a very different temporal profile, as shown in Fig. 4. We can see a very fast signal rise

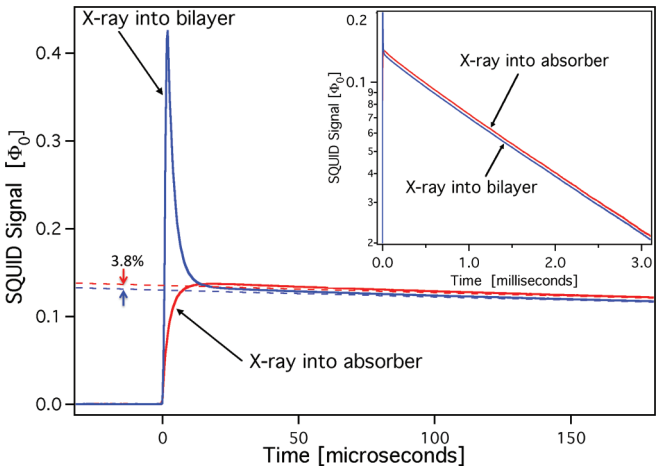

FIG. 4. (Color online) Temporal profiles of the Mn K α x-ray signals stopped in the absorber and in the bilayer. Inset is a plot of the same signals on an expanded time-scale, with a logarithmic scale for the signals.

($<1\mu$s) followed by an almost as fast initial decay ($\sim$2.7 μs) as the MPT film comes into quasithermal equilibrium with the absorber, and then the signal decays with the slower time constant associated with the microcalorimeter sensor plus absorber heat capacity. What is interesting is that although the slow time decay constant is identical for x-ray events into the absorber and the MPT film, the signal is measurably smaller when absorbed in the MPT film. By fitting to the regions of the temperature decays where there is just a single exponential decay we determined that the MPT absorption events are 3.8% $\pm$ 0.1% smaller. It is this difference in signal size that we interpret as mostly being the energy that is lost to the substrate through athermal phonons. One alternative mechanism for losing heat is due to the additional thermal conductance of heat out of the microcalorimeter due to the MPT film being at a higher temperature for a short duration. Knowing the heat capacities of the MPT film and absorber, and knowing the thermal conductances, we modeled this heat-loss path and determined that the additional amount of heat that is conducted away thermally is approximately 0.4% $\pm$ 0.1%. Thus we attribute the remaining 3.4% of the difference in signal heights as being due to energy loss via athermal phonons. In addition to the obvious difference in pulse shape over the first 2 μs there is a small departure of the two curves from simple exponential decays for approximately the first 100 μs after the absorber and bilayer have come into thermal equilibrium (represented by the dashed lines in Fig. 4).

III. THEORETICAL SIMULATION OF ENERGY LOSS AND SHAPE OF SPECTRAL LINES

The use of the term "athermal" phonons refers to a situation where phonons as well as all other excitations are far away from thermal equilibrium. This term, however, is too broad to properly describe the important features of a nonequilibrium phonon distribution. Nonetheless we adopt this terminology while discussing general concepts. This is not misleading because in all situations we characterize interacting phonons and electrons participating in the energy down-conversion

cascade in a complete way using time-evolving solutions of the appropriate kinetic equations.

The energy down conversion following the absorption of an energetic photon in a metal can be viewed as evolving through three distinct stages.[2–4,20] Stage I starts from the ejection of a photoelectron and proceeds through electron-electron (e-e) interactions, finishing with the formation of a highly nonequilibrium distribution of electrons and holes in the conduction band occupying a tiny volume in the vicinity of an absorption site. During stage I the entire photon energy is transferred from photoelectron to the ensemble of secondary, ternary, etc. electronic excitations with rapidly diminishing mean energy.

Stage II takes over when the mean energy of electronic excitations becomes sufficiently low for the electron-phonon (e-ph) interaction to determine further momentum and energy relaxation processes. This happens below a threshold E_1^*, i.e., $\epsilon \leqslant E_1^*$ where ϵ is the electron energy. For typical metals E_1^* far exceeds the Debye energy: $E_1^* \gg \Omega_D$. During this stage electrons and holes mostly relax via emission of phonons. As a result, a bigger fraction of photon energy is transformed into the energy of the evolving phonon distribution. Stage II is completed once the mean excitation energy reaches the low-energy threshold Ω_1, which is determined from the relation $\tau_{e\text{-ph}}(\Omega_1) = \tau_{\text{ph-}e}(\Omega_1)$. Below this threshold (stage III) a rapid energy conversion into predominantly electronic excitations takes place. The scenario described is correct provided the electron-electron interaction in the whole region $\epsilon \geqslant \Omega_1$ remains weaker than the electron-phonon interaction with spontaneous emission of a phonon, $\tau_{e\text{-}e}(\epsilon) \geqslant \tau_{e\text{-ph}}(\Omega_1)$. Whether this is true depends on material parameters and on the amount of disorder, which has a strong effect on the electron-electron interaction. We will consider both cases keeping the notation Ω_1 for the end point of the stage II accounting possible role of electron-electron interactions.

During stages I and III practically all the initial photon energy is stored within the electronic system and cannot be lost from the detector. In contrast with electronic excitations, phonons can easily escape through metal/dielectric interfaces. Therefore the only stage during which a significant energy loss may occur is stage II where athermal phonons carry most of the photon energy.

The simplest planar geometry that we will consider is shown in Fig. 5. The only possible phonon escape interface is at $z = -d/2$. The film is supposed to be grown on a solid substrate occupying the half space $z \leqslant -d/2$. Since $z = +d/2$ is a vacuum interface this is not an escape interface. There are several phenomena associated with escape of athermal phonons.[3]

First, the energy loss, $E_{\text{loss}}(z)$, is a function of the coordinate of an absorption site relative to the escape interface. We only show the z-coordinate dependence, where the z axis in Fig. 5 is in the direction normal to the film. Lateral coordinates are not important as long as photon absorption does not occur very close to the edges of the film. However, the z dependence is important determining the distance to the escape interface relative to mean-free paths of athermal phonons.

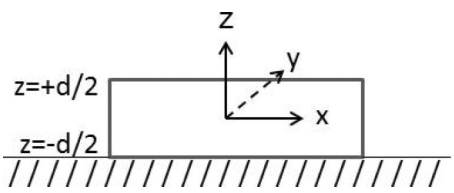

FIG. 5. Sensor film geometry.

Second, only phonons propagating inside the critical cone can pass through the interface, otherwise they are internally reflected. The existence of this restriction on transmission introduces statistical fluctuations to the loss of energy due to fluctuations in the number of phonons emitted into the critical cone. The statistical fluctuation in the number of escaping phonons contributes to a Gaussian fluctuation in the energy loss and can be viewed as an specific "athermal phonon noise," and thus can be added in quadrature with other statistically independent noise sources. These fluctuations are important for optical and near-infrared photons, but their effect becomes progressively small for x-rays.[20]

Finally, since the energy loss depends on the coordinate z, the distribution $P(z)$ of the x-ray absorption sites is an important factor determining the spectral lineshape. The lineshape depends on the x-ray energy and the angle of incidence.

A. Energy loss due to phonons of first generation

The phonon distribution of the first generation is established during the very fast electron down-conversion $E_1 \to \Omega_D$ and was found in explicit form in our earlier work. Energy loss due to the escape of phonons of the first generation created at the point of absorption at z_0 has the form[20]

$$E_{\text{loss},1}(z_0) = 4E \sum_{m=0}^{\infty} \frac{\kappa(m^2\zeta^2)\cos m\pi\,(1/2 + z_0/d)}{1+\delta_{m,0}} \times \int_0^1 d\xi\,\xi\,\eta(\xi)\Theta(\xi-\xi_c) \int_0^{\Omega_D} \frac{d\epsilon}{\Omega_D}\left(\frac{\epsilon}{\Omega_D}\right)^3 \times \frac{l_{\text{ph-}e}(\epsilon)}{d}\,\frac{[1-\exp(im\pi - d/l_{\text{ph-}e}(\epsilon)\xi)]}{1+m^2\pi^2 l_{\text{ph-}e}^2(\epsilon)\xi^2/d^2}, \quad (3)$$

where we denote $\kappa(x) = \exp(-x)\sinh(x)/x$, and define $\zeta^2 = \pi^2 D t_{dc}/2d^2$, D is the diffusion coefficient of down-converting electrons ($\epsilon \geqslant \Omega_D$), t_{dc} is the duration of $E_1^* \to \Omega_D$ stage and $l_{\text{ph-}e}(\epsilon)$ is the phonon mean-free path with respect to electronic reabsorption. The transmission coefficient $\eta(\xi)$ is a function of incidence angle, and $\xi_c = \cos\vartheta_c$, where ϑ_c is the critical angle.

We simplify the general expression (3) further. In what follows we use the linear dispersion relations for phonons taking $\omega_{\mathbf{q}} = cq$, where c is the velocity of sound and q is the phonon quasimomentum. In many low-temperature detectors such as TESs, MPTs, and MMCs the sensor film is either a normal metal or a superconductor operated close to the critical temperature T_c. Even in most other detectors such as STJs and MKIDs, which are operated at $T \ll T_c$, the lower-energy threshold of the phonon stage of down-conversion cascade satisfies the condition $\Omega_1 \gg \Delta$. Under this condition both electronic excitations and the matrix elements for the electron-phonon interaction are essentially the same as in a normal metal. Therefore we consider the asymptotical limit $\Delta \to 0$. In this limit the expression for the phonon lifetime due to

reabsorption by the electron system in metal is

$$\tau^{-1}_{\text{ph-}e}(\epsilon) = \frac{4\pi N(0)\alpha^2(\epsilon)\epsilon}{\hbar N}, \tag{4}$$

where $\alpha^2(\epsilon)$ is a coupling strength for the electron-phonon interaction entering the Eliashberg function $\alpha^2(\epsilon)F(\epsilon)$, $F(\epsilon)$ is the phonon density of states, $N(0)$ is the density of states per spin at the Fermi level, and N is the density of atoms. Although $\alpha^2(\epsilon)$ is a function of phonon energy and may exhibit variation over the phonon spectrum, the model becomes especially simple if we can use for it some averaged value. We thus introduce another model assumption taking $\alpha^2(\epsilon)$ as a constant, so that $\tau^{-1}_{\text{ph-}e}(\epsilon) \propto \epsilon$. In this case the last integral in the expression (3) has the form

$$Y(m,\beta,\xi) = \beta^4\xi^3 \int_0^{1/\beta\xi} dx x^4 \frac{1-\exp(im\pi - x)}{x^2 + m^2\pi^2}, \tag{5}$$

where $\beta = l_{\text{ph-}e}(\Omega_D)/d$. This integral can be explicitly calculated. It has the simplest form in the asymptotic limit $\beta \to 0$. Neglecting small terms of the order of $\exp(-1/\beta) \ll 1$ we obtain

$$Y(m,\beta,\xi) = \frac{\beta}{3}\Bigg\{1 - 3m^2\pi^2\beta^2\xi^2 - 3\beta^3\xi^3(-1)^m(2 - m^2\pi^2) + 3m^3\pi^3\beta^3\xi^3\Bigg[\arctan\left(\frac{1}{m\pi\beta\xi}\right) + \text{Si}(m\pi) - \frac{\pi}{2}\Bigg]\Bigg\}, \tag{6}$$

where $\text{Si}(x)$ is the integral sine function. Integration over ξ in the expression (3) is within the limits between ξ_c and 1. For acoustically soft metals on rigid substrates, ξ_c is close to unity and because the function $Y(m,\beta,\xi)$ depends smoothly on ξ it can be evaluated at $\xi = 1$. Introducing $\bar{\eta} = \int_0^1 d\xi\xi\eta(\xi)/\int_{\xi_c}^1 d\xi\xi$ and $p = \sin^2(\theta_c/2)$ we finally obtain the energy loss due to escaping phonons of the first generation in the form

$$E_{\text{loss},1}(z_0) = 4E\bar{\eta}p(1+\xi_c)\sum_0^\infty \kappa(m^2\zeta^2) \times \cos m\pi\left(\frac{1}{2} + \frac{z_0}{d}\right) Y(m,\beta,1). \tag{7}$$

In expressions (3) and (7) there are two separate factors that determine the magnitude of the loss: the probability of phonons to reach the escape interface (depending on intrinsic material properties), and the transmission characteristics of the interface.

B. Energy loss during $\Omega_D \to \Omega_1$ substage

The energy loss from the first generation of phonons may not be the dominant mechanism for energy loss because their mean energy is very high and so their mean-free paths are relatively short. For the same reason the first generation of phonons rapidly decays and after one to two generations asymptotically converges to the automodel solution of the kinetic equations describing the interaction between electrons and phonons. The details of this solution were discussed in our earlier work.[21]

Each subsequent phonon generation is characterized by a lower mean energy. In the first phonon generation the majority of phonons occupy states in the region of the highest density of states, i.e., close to the Debye energy. Thus the lifetime of the first generation of phonons is roughly $\tau_{\text{ph-}e}(\Omega_D)$. The absorption of one of these phonons creates two electronic excitations with mean energy of $\Omega_D/2$. The lifetime of electrons in metals with respect to the spontaneous emission of a phonon is

$$\tau^{-1}_{e\text{-ph}}(\epsilon) = \frac{2\pi}{\hbar Z(0)}\int_0^\epsilon d\Omega\alpha^2(\Omega)F(\Omega), \tag{8}$$

where $Z(0)$ is the renormalization factor of a metal. For $\epsilon \geqslant \Omega_D$ we obtain $\tau^{-1}_{e\text{-ph}}(\epsilon) = \tau^{-1}_{e\text{-ph}}(\Omega_D) = \tau_s$ and this time does not depend on electron energy. For $\epsilon \leqslant \Omega_D$ and assuming α^2 is a constant value, $\tau^{-1}_{e\text{-ph}}(\epsilon) \propto \epsilon^3$ for the Debye model of the phonon spectrum. From this estimate it follows that the intermediate electrons (holes) will diffuse during their average survival time, i.e., $\tau_{e\text{-ph}}(\Omega_D/2) = 2^3\tau_s$.

Another important factor is the evolution of the electron diffusivity. During the stage $E_1^* \to \Omega_D$ the electron momentum relaxation is determined by the combined action of elastic scattering and electron-phonon scattering with the rate $\tau^{-1} = \tau_i^{-1} + \tau_s^{-1}$. The intermediate electrons have a typical energy of $\Omega_D/2$; they emit lower-frequency phonons of the second generation and therefore are scattered less efficiently. For these electrons $\tau^{-1}(\Omega_D/2) = \tau_i^{-1} + \tau_s^{-1}/2^3$ so that $D' \geqslant D$, where D' is their diffusion coefficient. This diffusion coefficient is faster than for electrons with $\epsilon \geqslant \Omega_D$ resulting in a much greater spread of phonons of the second generation. The extent of spatial spread can be evaluated by comparing the factor Dt_{dc} for the first generation of phonons with $8D'\tau_s$ for the second.

The accurate evaluation of the contribution of the second-generation phonons to energy loss, fluctuations, and spectral lineshape is difficult. As we will see below, most of the energy loss occurs at an advanced stage of the $\Omega_D \to \Omega_1$ cascade. Starting with the decay of phonons of the first generation, the phonon distribution rapidly converges to an asymptotic automodel solution.[2] The automodel solution at least partially takes into account contributions from the second-phonon generation. The dominant role of the $\Omega_D \to \Omega_1$ stage in energy loss arises because, as the mean phonon energy decreases, more phonons are likely to reach the escape interface. In contrast, phonons of the first generation make a dominant contribution to fluctuations of the energy loss and asymmetry of the spectral lineshape. In metals with a long $\Omega_D \to \Omega_1$ stage, i.e., $\Omega_D \gg \Omega_1$, we expect the automodel solution to be a good approximation. It is only in the situation when the strong inequality $\Omega_D \gg \Omega_1$ is not fulfilled that contributions from second phonon generations may be needed.

An expression for $E_{\text{loss},\Omega_D\to\Omega_1}$ can be written as

$$E_{\text{loss},\Omega_D\to\Omega_1} = E\eta p\frac{1+\xi_c}{2}\frac{12Z(0)}{11Z(0)+3}\beta g\left(\frac{\Omega_D}{\Omega_1}\right), \tag{9}$$

where

$$g(x) = x\int_{1/x}^1 \frac{dz}{z} f(z)\Bigg\{\text{Ei}(1,z(x-1)) - \text{Ei}(1,1-z) + \exp(z)[\text{Ei}(1,1) - \text{Ei}(1,xz)] + \ln\frac{x-1}{x(1-z)}\Bigg\},$$

with Ei(a,z) being the exponential integral and

$$f(z) = 1 - z - \frac{z}{12}\{z^2[\cos\sqrt{2}\ln z - 7\sqrt{2}\sin\sqrt{2}\ln z] - 1\}.$$

In Eq. (9) we kept only spatially homogeneous contributions and neglected all spatially varying terms in the general solution,[21] which are not important. The order of magnitude of the neglected terms is $d^2/[\pi^2 D\tau_{\text{ph-}e}(\Omega_D)]$, which is much less than unity for all realistic situations.

Combining all results we finally arrive in the total energy loss from our sensor film

$$E_{\text{loss}}(z_0) = E_{\text{loss},1}(z_0) + E_{\text{loss},\Omega_D\to\Omega_1}, \tag{10}$$

where the first contribution is strongly dependent upon the z coordinate of the absorption site, while the second contribution is highly insensitive to such a dependence. The magnitudes of both contributions are determined by the effective transmission coefficients for the first and subsequent generations of phonons and by the extent of the $\Omega_D \to \Omega_1$ substage of the stage II down-conversion cascade. In an ideal film the second contribution can be the largest and is determined by the intrinsic properties of the film material. In real films the duration of the $\Omega_D \to \Omega_1$ substage may become significantly shortened by a strong elastic scattering enhancing electron-electron interaction. The dependence of $E_{\text{loss},\Omega_D\to\Omega_1}$ on the parameter Ω_1/Ω_D is illustrated in Fig. 6. This dependence is strong, so that the relative contributions of the first and subsequent phonon generations to the total energy lost is sensitive to the strength of the electron-electron interaction.

Finally, the integrands in expressions (3) for $E_{\text{loss},1}(z_0)$ and the function $g(x)$ for $E_{\text{loss},\Omega_D\to\Omega_1}$ in Eq. (9) give the spectral distribution of athermal phonons escaping from a metal film into a substrate. There are many physical situations where this information may be important. Here we mention just two examples: The first is in calculating the amount of energy back-flow into a thermalizing metal film. Due to the strong elastic scattering in the substrate (either isotope related or due to disorder), the back-scattered phonon flux depends upon the energy of athermal phonons. It can be evaluated provided that the spectral distribution of escaping phonons is known. In special cases this energy back flow may ultimately affect the energy loss from the film. A second example is in quantifying the thermalization or energy down-converting properties of thin metal films grown on the surfaces of semiconductors or dielectrics where there is an incident flux of high-energy phonons. In this situation the excitations that are generated within the metal film are induced by the incident athermal phonon flux. With a slight modification to the initial phonon distribution in the film, the quantitative relations for spectral transformations of the reflected flux relative to the incident flux can be derived.

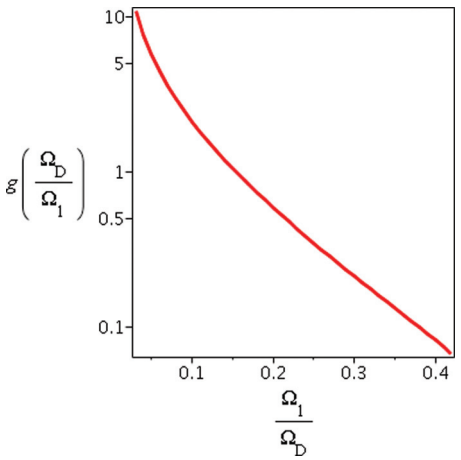

FIG. 6. (Color online) Dependence of $E_{\text{loss},\Omega_D\to\Omega_1}$ on low threshold Ω_1/Ω_D.

C. Spectral lineshape

In the previous subsections we presented several important asymptotical results derived from the general expressions as preliminary material for the original development below. In this subsection we start discussing modeling of the spectral lineshape.

This topic in the area of low-temperature detectors so far has been restricted to a very limited number of cases; namely, detectors with a spatially homogeneous response where the spectral lineshape is Gaussian, and spatially inhomogeneous STJs where the standard approach was fitting the experimental data with a skewed Gaussian allowing the variance to depend on energy. Systematic attempts to study the role of spatial inhomogeneities in lateral directions and to simulate the effects of quasiparticle losses at the edges or in the leads or local defects have been reported in several works both experimental[22–24] and theoretical.[25–28] The only theoretical simulation of the spectral lineshape[28] in laterally inhomogeneous detectors has revealed that spectral lineshape is sensitive to the details of energy loss.

In the nearly ideal detectors which we discuss in this paper we focus our attention on the fundamental z dependence of E_{loss} and ignore the less fundamental potential effects of lateral inhomogeneity. The only discussion of the role of "vertical" inhomogeneities on worsening of the FWHM, when fitting the experimental lines with a skewed Gaussian, is available in Kozorezov *et al.*[20] We will demonstrate below in Secs. IV and V that further development of the model aimed at simulation of spectral lineshape of a nearly ideal detector is possible and desirable. It becomes very informative because of the sensitivity of detector response to details of energy deposition and loss.

In the ideal situation when there is no energy loss, $E_{\text{loss}} = 0$, the normalized spectral lineshape $S(E)$ is Gaussian, $\int_{-\infty}^{\infty} dE\, S(E) = 1$,

$$S(E) = \frac{1}{\sqrt{2\pi}\sigma}\exp\left[-\frac{(E-E_0)^2}{2\sigma^2}\right]. \tag{11}$$

The line is centered around photon energy E_0, and its full width at half maximum is $2\sqrt{2\ln 2}\sigma$. If $E_{\text{loss}}(z_0) \neq 0$, then the lineshape is

$$S(E,z_0) = \frac{1}{\sqrt{2\pi}\sigma}\exp\left\{-\frac{[E-E_0+E_{\text{loss}}(z_0)]^2}{2\sigma^2}\right\}, \tag{12}$$

provided that an absorption takes place at a site with fixed coordinate z_0. If $P(z_0,E_0)$ is the normalized $[\int dz_0 P(z_0,E_0) = 1]$ distribution function of absorption sites at a depth z_0 for a photon energy E_0 then the spectral lineshape is given by the

convolution

$$\bar{S}(E) = \int_{\text{detector}} dz_0 P(z_0, E_0) S(E, z_0).$$

The lineshape due to absorption events in the sensor film is

$$\bar{S}(E) = \int_{-d/2}^{d/2} dz_0 P_s(z_0, E_0) S(E, z_0), \tag{13}$$

where the distribution of absorption sites in the sensor for x-rays incident onto the $z = +d/2$ interface is

$$P_s(z_0, E_0) = \frac{\exp[(z_0 - d/2)/L(E_0)]}{L(E_0)\{1 - \exp[-d/L(E_0)]\}}, \tag{14}$$

where $L(E_0)$ is the $1/e$ photon absorption depth. Finally, if the source is not monochromatic, an extra straightforward convolution with its spectral density is needed.

IV. MODELING SPECTRAL LINESHAPE AND ENERGY LOSS FROM X-RAY ABSORPTION EVENTS IN MO/AU FILM

In this section we concentrate on modeling the spectral lineshape and energy loss from x-ray absorption events in a Mo/Au film. In soft x-ray range the role of fluctuations on spectral lineshape was shown to be generally small.[20] For soft x-rays at 6 keV using the expression J for fluctuation factor,[20] we estimate the variance due to fluctuations in the number of escaping phonons of the first generation for the Mo/Au sensor to be $\sigma_f \leqslant 1.0$ eV. For all purposes of this work this is small and can be neglected.

The two different experiments described in Sec. II allow us to probe different physical parameters of the film. In particular, energy loss is mostly sensitive to the duration of stage II and transmissivity of the escape interface, but not to the size and position of the initial phonon bubble (first generation of phonons) relative to the escape interface. In contrast, the spectral lineshape is sensitive to both the size and the position of a phonon bubble. Another aspect to consider is that phonon transmission may be strongly assisted by scattering if there is significant roughness of the interface. Fitting the model predictions to both sets of data potentially reveals details of the energy that is transferred across the escape interface by athermal phonons over a broad frequency range. It also allows us to evaluate the strength of the electron-electron interaction relative to the electron-phonon interaction in metals, both in the high-excitation-energy range, from a few eV down to the Debye energy above the Fermi level, and at much lower energies close to equilibration. These insights, apart from their obvious practical implications for single-photon low-temperature detectors, also have more fundamental importance for characterizing the interactions in highly excited metals and the equilibration process over a much wider spectral range than those previously accessible with other experiments.

A. Definitions of down-conversion stages I and II in Au and Mo

In our modeling, we start from the time during stage I when the e-ph interaction becomes stronger than the e-e scattering. This happens at the threshold E_1 determined from the condition $\tau_{e\text{-}e}^{-1}(E_1) = \tau_s^{-1}$. In our earlier work[2] we considered the metal to be sufficiently pure that, for E_1 in the eV range above the Fermi energy, the e-e scattering could be considered as in ideal metal and to not be affected by disorder. However, in thin films with residual resistivity ratios (RRRs) less than 10 it is often the case that elastic scattering times for electrons, τ_{imp}, either due to bulk scattering or diffuse scattering at surfaces or interfaces, are of the same order of magnitude as τ_s. Correspondingly, at the energy E_1, the electron-electron scattering is significantly affected by elastic scattering. In this energy range single–electron-phonon scattering events are quasi-elastic and also contribute to elastic scattering. The effect of elastic scattering on electron-electron interactions depends on the system dimensionality.[29] The criterion for the normal direction of the film of thickness d to not contribute to the dimensionality[30] is $d < \sqrt{\hbar D/\epsilon}$. For the lowest energies of interest, $\epsilon \geqslant \Omega_1$, the system becomes two-dimensional in the context of e-e scattering only if $d < \sqrt{\hbar D/\Omega_1}$. Thus we expect that, even for small thresholds $\Omega_1 \ll \Omega_D$, unless the film is very thin it is still three-dimensional for most of the $\Omega_D \to \Omega_1$ interval so that $\tau_{e\text{-}e}^{-1}(\epsilon) \propto \epsilon^{3/2}$. At the same time both impurity and electron-phonon scattering times in this energy range may be taken to be independent of energy. As a rough estimate we scale $\tau_{e\text{-}e}^{-1}(\epsilon)$ up in energy according to the $\epsilon^{3/2}$ law until it becomes as big as $\tau_{\text{imp}}^{-1} + \tau_s^{-1}$. We thus redefine E_1 so that in less-pure metals it sets the threshold below which electron momentum scattering is controlled by impurities and phonons:

$$\tau_s^{-1} + \tau_{\text{imp}}^{-1} = \tau_{e\text{-}e}^{-1}(E_1) = a\tau_{e\text{-}e,\text{ideal}}^{-1}(E_1) = a\frac{E_1^2}{\hbar E_F}\left(\frac{r_s^{1/2}}{7.96}\right), \tag{15}$$

where E_F is the Fermi energy, r_s is the radius of a sphere in atomic units which encloses one electron charge, and $a > 1$ is a numerical factor that takes into account that at E_1 the disorder scattering slightly enhances the e-e scattering relative to the ideal situation. The last term in Eq. (15) is the expression for the e-e scattering rate in an ideal metal.[31]

At the end of stage I at an energy E_1^* the electron-phonon scattering also becomes a dominant source of energy relaxation. The latter can be found from the equation[32]

$$\tau_{e\text{-}e}(E_1^*) = \frac{2E_1^*}{3\Omega_D}\tau_s. \tag{16}$$

The meaning of this balance is that, over the duration of the time equal to $\tau_{e\text{-}e}(E_1^*)$, the probability of having the electron energy relaxed by a factor 3 in the e-e scattering process (splitting the initial energy E_1^* equally between the three electronic excitations after e-e iteration) is the same as for the process of sequential emission of the $2E_1^*/(3\Omega_D)$ Debye-energy phonons. Taking $\tau_{e\text{-}e}^{-1} = \tau_{e\text{-}e}^{-1}(E_1)(E_1^*/E_1)^{3/2}$ and using Eqs. (15) and (16) we obtain

$$E_1^* = \Omega_D \left(\frac{13.67}{r_s^{1/2}}\frac{\hbar E_F}{\tau_s \Omega_D^2}\right)^{3/10}\left(\frac{a}{1 + \tau_s/\tau_{\text{imp}}}\right)^{1/10}. \tag{17}$$

To estimate the duration of the down-conversion stage from E_1 down to Ω_D we first evaluate the duration of $E_1 \to E_1^*$, i.e., $t_{dc}(E_1 \to E_1^*)$. Assuming that with each e-e scattering event the energy of electrons decreases by a factor of 3, we must sum the geometric progression with the scale factor $3^{3/2}$. Thus

$t_{dc,E_1\to E_1^*} < \tau_{e\text{-}e}(E_1^*)/(3^{3/2}-1)$. This is an upper limit to the estimate because the geometric progression must be truncated due to the finite ratio E_1/E_1^* and weaker parallel phonon emission also takes place. Below E_1^* the relaxation down to a level $E_1^*/3$ occurs over the duration $\tau_{e\text{-}e}(E_1^*)/2$ with the e-e and e-ph scattering processes at E_1^* contributing equally. Further relaxation from $E_1^*/3$ to Ω_D lasts for another $\tau_{e\text{-}e}(E_1^*)/2$ only taking into account phonon scattering. Combining all of these estimates we have $t_{dc} < [1/(3\sqrt{3}-1)+1]\tau_{e\text{-}e}(E_1^*) \approx 1.24\tau_{e\text{-}e}(E_1^*) \approx (E_1^*/\Omega_D)\tau_s$.

More detailed studies of the down-conversion stages I and II require estimates of the electron-phonon coupling strength in the bilayer. In practice this is very difficult to analyze. Indeed, gold belongs to a class of weakly coupling metals, while molybdenum belongs to the intermediate-coupling metals. We will make estimates for Au and Mo separately before hypothesizing about the appropriate parameter values for the Au(330 nm)/Mo(50 nm) bilayer.

We first estimate τ_s. Taking $\tau_s = \tau_{e\text{-ph}}(\Omega_D)$ from Eq. (8) and using the experimentally measured Eliashberg function $\alpha^2(\Omega)F(\Omega)$ for gold[33] we obtain $\tau_s \approx 0.13$ ps. A similar estimate for molybdenum based on the calculated Eliashberg function[34] yields $\tau_s \approx 0.030$ ps. Thus, t_{dc} in Mo is likely to be a factor of 4 faster than in Au assuming roughly the same ratio E_1^*/Ω_D, [in Mo, $\Omega_D = 33$ meV, and the combination $\tau_s\Omega_D^2$ in Eq. (17) is nearly the same for both materials].

In order to evaluate $\tau_{\text{ph-}e}(\Omega)$ we use expression (4). Assuming $\alpha^2(\Omega)$ to be a constant value and expressing it in terms of the first reciprocal moment of the Eliashberg function λ (mass enhancement factor), in the Debye approximation we obtain

$$\tau^{-1}_{\text{ph-}e}(\epsilon) = \frac{4\pi N(0)\Omega_D}{9N}\lambda\epsilon. \tag{18}$$

The accuracy of this approximation is known not to be high. However, it is unlikely to be worse than the use of the one-branch nondispersive phonon-spectrum model that we adopted at the beginning. The use of expression (18) yields $\tau^{-1}_{\text{ph-}e}(\epsilon) = \tau_{\text{ph-}e}(\Omega_D)\frac{\epsilon}{\Omega_D}$. In the same approximation we obtain from (8) $\tau_{e\text{-ph}}(\epsilon) = \tau_s(\frac{\epsilon}{\Omega_D})^3$. Combining the two results we obtain

$$\Omega_1 = \Omega_D\sqrt{\tau_s/\tau_{\text{ph-}e}(\Omega_D)}. \tag{19}$$

This expression with $\tau_{\text{ph-}e}(\Omega_D)$ taken from Eq. (18) turns out to be close to the one obtained directly from $\tau^{-1}_{\text{ph-}e}(\Omega_1) = \tau^{-1}_{e\text{-ph}}(\Omega_1)$ and using Eqs. (4) and (8). Then assuming $\Omega_1 \ll \Omega_D$ and taking for $\alpha^2(\Omega)$ its limiting value $\alpha^2(0)$ and approximating $F(\Omega)$ by its Debye value, which is accurate in this frequency range, we finally obtain

$$\Omega_1 = \Omega_D\sqrt{\frac{2}{3}\frac{N(0)\Omega_D}{N}(1+\lambda)}. \tag{20}$$

This is a better approximation than Eq. (19) because the only assumption used for its derivation is $\alpha^2(\Omega_1) = \alpha^2(0)$. For Au we obtain $\Omega_1/\Omega_D = 0.036$ and 0.039 from Eqs. (19) and (20), respectively. For Mo we obtain from Eq. (20) $\Omega_1/\Omega_D = 0.12$, which sets a higher threshold than Ω_1 in gold.

Using for an estimate the numbers for Au as a weaker-coupled e-ph system, $E_F = 5.51$ eV, $\Omega_D = 14.2$ meV, $r_s = 3.0$, and $\tau_s = 130$ fs, we obtain $E_1^*/\Omega_D \approx 8.2$ neglecting the last term in Eq. (17) and $E_1/E_1^* \approx 4.0[a^{-1}(1+\tau_s/\tau_{\text{imp}})]^{3/5} \simeq 4.0$. The duration of $E_1 \to \Omega_D$ stage therefore is $t_{dc} \leqslant 0.8$ ps.

B. Modeling the bilayer

The model parameters determining the phonon loss and spectral lineshape are Ω_1/Ω_D, $L(E)$, D, t_{dc}, $\beta = l_{\text{ph-}e}(\Omega_D)/d$, and η_{eff}. The first group are the parameters depending on the bulk properties of sensor. The diffusion coefficient D of down-converting electrons and t_{dc} enter in combination Dt_{dc} as a single parameter defining the size of the excited volume filled with the first generation of phonons. During the $E_1^* \to \Omega_D$ down-conversion stage, the diffusion coefficient of a bilayer is modified by strong elastic scattering due to phonon emission, so that $D = D(0)/(1+\tau_{\text{imp}}/\tau_s)$, where $D(0)$ is the measured low-temperature value. The x-ray absorption depth $L(E)$ and correspondingly distribution function of absorption sites $P_s(z_0,E)$ is modeled in a piecewise way to incorporate the discontinuity of x-ray absorption in a bilayer. This is necessary to account for the factor ~2.5 difference in x-ray absorption efficiency in Au and Mo. The parameter η_{eff} is of special importance. It depends on bulk properties such as the acoustic impedances of both the sensor film and the substrate. It also depends on the properties of the sensor to substrate interface.

1. Ideal interface

For ideal atomically clean interfaces without phonon scattering, η, p, and ξ_c can be calculated using the acoustic mismatch model (AMM) of the elastic isotropic continuum.[35] This model allows us to evaluate the average transmission coefficients for phonons of individual polarizations which are incident from the metallic side onto the horizontal interface with the substrate. There are two shear waves with horizontal and vertical displacements, SH and SV, respectively, and a longitudinal L wave. AMM coefficients are useful in defining the probable range for phonon transmission of longer-wavelength phonons depending upon the elastic impedances of the metal and substrate and the angles of total internal reflection for individual modes. We will use the one-mode model of the phonon spectrum and take the sound velocity c of the metal to be equal to that entering the Debye model, i.e., $3/c^3 = 2/c_t^3 + 1/c_l^3$, where c_t and c_l are sound velocities for transverse and longitudinal phonons, respectively. Similarly, for the substrate we use c_s which is expressed using the same relation through respective sound velocities c_{st} and c_{sl}. Furthermore we assume that c is significantly smaller than c_s, so that the angle of total internal reflection $\theta_c = \arcsin(c/c_s)$ is small. Under these conditions we approximate η as for SH waves[35] and $p = \sin^2\frac{\theta_c}{2}$. We stress that the actual product $\eta p(1+\xi_c)/2$ entering the energy loss and affecting the spectral lineshape is a fitting parameter to be found from fitting the theoretical E_{loss} and lineshape to experiment, thus such an estimate serves as a consistency check.

2. Rough interface

The transmission of higher-frequency phonons requires a special analysis. The first generation of phonons peaks at the maximum of the phonon density of states. Thus,

the characteristic energy is $\simeq\Omega_{\rm D}$. The transmission of these phonons may significantly differ from the AMM predictions. For a sufficiently rough interface, phonon transmission is better approximated by the diffuse mismatch model (DMM).[36] In fact, the real transmission lies between the two estimates.[37,38] In the case of roughness scattering the expression (7) also can be used, but the factor $\eta p(1+\xi_c)/2$ must be replaced by an effective transmission coefficient $\eta_{\rm eff}$. A significant difference between the two limiting cases arises because of different physical mechanisms of phonon transmission. For an ideal interface the AMM transmission properties are determined by the bulk characteristics of the sensor and adjacent media, i.e., acoustic impedances. For scattering-assisted phonon transfer across the interface, the transmission becomes strongly dependent on the correlation scales of the interface roughness. Therefore, the transmission characteristics for first-generation phonons and longer-wavelength athermal phonons of subsequent generations may strongly differ. The most important distinction is not only in quantitative differences resulting in differences in magnitudes of transmission but also that, in scattering-assisted phonon transmission of short-wavelength phonons, the interface roughness is being probed locally and thus the transmission coefficient may fluctuate from point to point along the interface. Thus, $E_{{\rm loss},E_1^*\to\Omega_{\rm D}}$ will contain a stochastic component dependent on lateral coordinates and will introduce an extra broadening to the spectral lineshape.

C. "Effective-medium" model

The simplest model for considering phonon transport in a bilayer is that of the effective medium, which is a single layer with thickness d the same as the thickness of the Mo/Au bilayer but with phonon characteristics being intermediate between those of Au and Mo. For example, we may let c vary between $1.4\times10^5\leqslant c\leqslant 3.7\times10^5$ cm/s; the lower limit being the average sound velocity for Au and the upper limit being that for Mo. The athermal phonons entering from Au into Mo layer interact with electrons in Mo stronger than in Au so that phonons can further down convert even in the small-thickness layer of Mo. The down-conversion process in Mo is no different than that described above for Au, and hence we may also discuss down conversion in the effective medium in terms of effective parameters having values intermediate between those in Au and Mo. There exists a slight problem connected with a small number of cases of x-ray absorptions in Mo: Phonons of the first generation in Mo above $\Omega_{\rm D,Au}$ in gold (we added extra reference to Au to emphasize that this quantity relates to gold) cannot enter and propagate in Au and hence cannot be described in the framework of the effective-medium model. However, these phonons in Mo ($\sim$33 meV) decay very fast and may be disregarded on their own. Their decay products, the subsequent generations of athermal phonons in Mo, fall below $\Omega_{\rm D,Au}$ and may be considered within the model of an effective homogeneous single layer.

D. "Effective-interface" model

An alternative model can be also suggested. In this model we completely ignore x-ray absorptions in the Mo layer for the Au(330 nm)/Mo(50 nm) bilayer. The absorption coefficient in Mo at 6 keV is a factor of 2.4 smaller than in Au. With the thickness of the Mo layer being $\sim0.13d$ only 6.9% of the x-ray photons are absorbed in the Mo. The role of Mo layer in this model is in modifying the transmission characteristics of phonons at the Au/Si interface. In this sense the Mo layer plays the role of an effective interface. The properties of an effective interface are determined by the strong e-ph interaction in Mo. From Eq. (18) we obtain for Mo layer $\tau_{\text{ph-}e}(\Omega_{\rm D})=1.7$ ps and $\tau_{\text{ph-}e}(\Omega_1)=15$ ps. Therefore the mean-free paths for phonons with $\Omega\simeq\Omega_{\rm D,Au}$ are short in comparison with the thickness of the Mo layer and these phonons entering Mo from the Au layer are reabsorbed and further experience enhanced down conversion in Mo. A rough estimate for the effective transmission coefficient to be used instead of $\eta p(1+\xi)/2$ in expression (7) can be taken as

$$\eta_{\rm eff}=\frac{\eta_{\rm Au/Mo}p_{\rm Au/Mo}(1+\xi_{\rm Mo/Au})/2}{1+\tau_{\rm esc,Mo/Si}/\tau_{\rm esc,Mo/Au}}. \tag{21}$$

This expression reflects the balance of the flux incoming from Au into Mo with the outgoing phonon fluxes from Mo into gold and Mo into the Si substrate. The ratio of the latter is taken as the ratio of phonon escape times from the Mo layer of thickness $d_{\rm Mo}$ via the respective interfaces, $\tau_{\rm esc,Mo/Au}=4d_{\rm Mo}/(\eta_{\rm Mo/Au}c_{\rm Mo})$ and similarly for the escape into the Si substrate, and is equal to the ratio $\eta_{\rm Mo/Au}/\eta_{\rm Mo/Si}$.

V. MODELING SPECTRAL LINESHAPE IN MO/AU SENSOR FOR MN Kα COMPLEX

The energy loss from a thin film is given by the expression (10). If the source of x-rays is monoenergetic at a photon energy E_0, then the lineshape is determined by the coordinate-dependent part of $E_{\rm loss}(z_0)$. As was determined from expressions (7) and (9), $\frac{dE_{\rm loss}(z)}{dz}|_{\pm d/2}=0$. This is a consequence of the phonon distribution being related to the local density of diffusing electrons which are characterized by zero flux at the interfaces with vacuum or dielectric. For $\sigma\to0$ we have $S(z,E_0)\to\delta(E-E_0+E_{\rm loss}(z))=\delta(z-z^*)/|E'_{\rm loss}(z^*)|$, where $z^*(E)$ is the solution of $E-E_0+E_{\rm loss}(z)=0$. Due to the presence of the derivative in the denominator there appears an integrable singularity at $E=E_0+E_{\rm loss}(\pm d/2)$ resulting in a characteristic "double-peak" or shoulder in the lineshape, as depicted in Fig. 7. The left

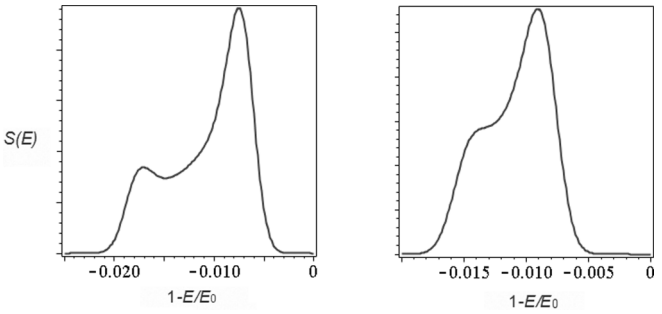

FIG. 7. Two calculated spectral redistributions, given in terms of probability versus energy, due to the energy loss in a thin film from a monoenergetic photon source. The double-peak lineshape (arbitrary units) depends upon the film material parameters, and two examples are shown.

TABLE I. Model parameters for Au film.

τ_s ps	$\tau_{\text{ph-}e}(\Omega_D)$ ps	$c \times 10^5$ cm/s	σ eV	η_{eff}	D cm^2/s	t_{dc} ps
0.13	80	1.4	4.15	0.035	500	0.75

and right panels of Fig. 7 correspond to different material parameters.

We model our experimental results using the Holzer spectrum[39] for the Mn Kα complex. The double-peak structure will be present for all components of the Holzer spectrum. Therefore, the resulting lineshape is more complicated and contains more features. These features, however, may be significantly smeared if the baseline resolution described by the variance σ is not sufficiently high. Below we describe in detail simulation of the lineshape using the effective-interface model to describe Mo/Au bilayer. Table I shows all parameters used for the lineshape simulation.

The choice of parameters has been discussed in the previous section. For η_{eff} in Table I we show the AMM estimate for Au/Mo interface reduced by the fitting factor 2 (see below) to account for the role of the denominator in Eq. (21). Figure 8 shows the results of the simulation together with a breakdown of the overall spectrum into contributions from different depths of the 330 nm Au film, i.e., from four different notional 82.5-nm-thick sublayers. The outermost left line is for the sublayer which neighbors the Mo layer and shows the highest loss. This is followed by successive sublayers at larger distances from the escape interface and therefore smaller respective losses. Figure 9 shows the simulated line superimposed upon the experimental result.

When we compare our simulated curve with the experimental data it is apparent that both have approximately the same FWHM. Thus the dependence of energy loss on the coordinate of the absorption site results in line broadening, which is roughly in agreement with the experiment. The simulated lineshape shows a significantly different behavior on both sides of the peak and also a well-defined shoulder. The origin of the shoulder was discussed above and is clear from Fig. 8. The experimental line exhibits a longer tail on the lower-energy side and also a much smoother drop on the left side of the

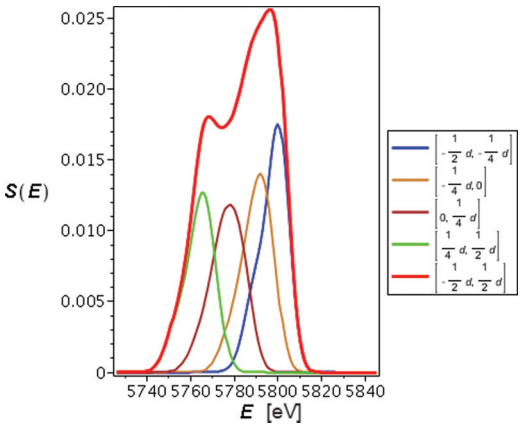

FIG. 8. (Color online) Simulated normalized lineshape including the contributions from absorption within different depth regions of the Au film.

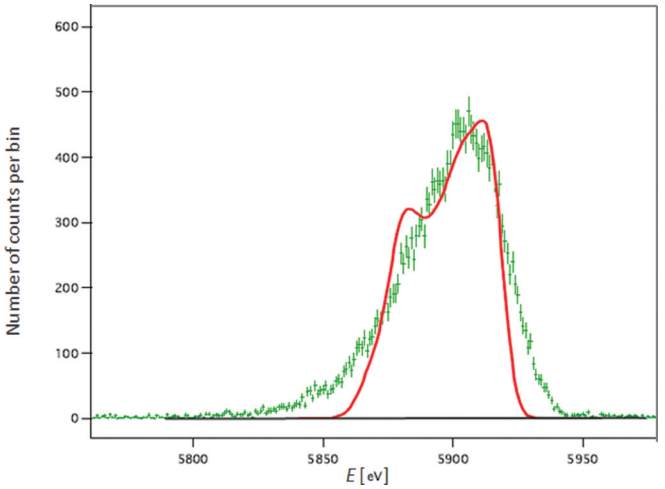

FIG. 9. (Color online) Comparison of simulation line andinterface experiment.

peak. The theoretical curve also exhibits a rapid decrease on the right-hand side of the peak, with this drop occurring over 10 to 15 eV, in contrast with the measured spectrum, which has a much slower decrease in number of counts with energy.

The lower-energy tail is easier to interpret within the model of energy loss from the Au/Mo film. Absorptions in Mo typically result in a bigger loss from the Mo film. This is not only due to the closeness to the escape interface, but also to the better acoustic matching to the Si substrate. The additional broadening to lower energies in Fig. 9 can also be explained because the distribution function $P_s(z_0, E)$ for a bilayer has not yet properly been taken into account. It can be written in the form

$$P_s(z_0,E) = \frac{\Gamma_{\text{Au}}\exp(-\Gamma_{\text{Au}}d)}{1-\exp(-\Gamma_{\text{Au}}d_{\text{Au}}-\Gamma_{\text{Mo}}d_{\text{Mo}})} \times\left[\exp(-\Gamma_{\text{Au}}z_0)\Theta(d/2-z_0)\Theta(z_0+d/2-d_{\text{Mo}}) + \frac{\Gamma_{\text{Au}}}{\Gamma_{\text{Mo}}}\exp(-\Gamma_{\text{Mo}}z_0)\Theta(z_0+d/2)\Theta(d_{\text{Mo}}-d/2-z_0)\right], \quad (22)$$

accounting for the weaker absorption in Mo relative to Au. This will reduce the weight of the smallest (left) peak in Fig. 8 (due to absorptions close to the escape interface), down by a factor of 2.4.

It is not possible to explain the higher-energy side of the peak profile within either of the two models. With the experimental baseline resolution $\sigma = 4.15$ eV and the intrinsic distribution of Mn K α x-rays (as described by Holzer) extending over just 10 eV, there are no physical reasons within our model of phonon losses to have this profile less steep than 10 to 15 eV.

In order to understand the leading-edge discrepancy we have examined the phonon escape from the sensor in more detail. As we have seen, the spectral lineshape is sensitive to both the bulk-phonon transport characteristics and the transmission across interfaces. Simplifications in modeling the bulk-phonon transport cannot be responsible for the failure

to correctly reproduce all the major features of the spectral lineshape. More realistic models of the phonon spectrum and the evolution of phonon distributions will only slightly modify the statement that the first generation of down-conversion phonons has a dominant effect on spectral lineshape, while subsequent generations, due to their fast spatial spread, only contribute to the height of the peak and its horizontal shift (total energy loss). Our derivation of the distribution function for the first generation of phonons can be generalized to a spectrum containing three acoustic branches. A generic feature of this distribution function is that it forms as a result of spontaneous emission of phonons by down-converting electrons during the $E_1^* \to \Omega_D$ stage, when electrons are capable of emitting all phonons. It is also important that the lifetimes of all phonons emitted are much larger than the duration of this stage. As a result, the first phonon generation distribution function is a snap-shot of the distribution of phonons at a time $t = t_{dc}$. The details of this distribution are determined by the densities of states at each energy together with the Eliashberg coupling functions for individual modes to determine the relative magnitudes. The more complicated three-branch bulk model is capable of changing the structure on the left-hand side of the measured x-ray spectrum by splitting the shoulder into individual features due to loss of transverse and longitudinal phonons. However, it is unlikely that this structure will be smooth and it definitely cannot introduce a smoother variation for the higher-energy side of the x-ray spectrum. On the left, the spectrum begins from x-ray absorption from $E = E_0 - E_{\text{loss}}(-d/2)$, while on the right it terminates at $E = E_0 - E_{\text{loss}}(d/2)$.

The origin of the discrepancy between the model and data is most likely to be connected with the transmission characteristics of phonons of the first generation whose escape determines the spectral lineshape. So far we have shown the results of simulations in Figs. 8 and 9 assuming coherent transmission of phonons across the ideal interface. Phonons of the first generation in Au have energies close to Ω_D, corresponding to maxima in the phonon density of states in Au of 6 to 8 meV for transverse and 12 to 14 meV for longitudinal phonons. The wavelengths of these phonons are on the nanometer scale so that any roughness of the interface on the nanometer scale will cause strong phonon scattering. The transmission of the first-generation phonons $\leqslant \Omega_{D,Au}$, which are incident onto the Au/Mo interface from gold, is more strongly affected by the roughness than the transmission of the same-frequency (but larger-wavelength) phonons which are incident on the same interface from the molybdenum side. Moreover in the effective-interface model of Mo/Au bilayer phonons inside Mo layer experience more effective down conversion and therefore at any moment of time will have lower mean frequencies. Thus, the phonon transmission across the Au/Mo interface (from Au to Mo) may be determined by its roughness while at the same time transmission of phonons across the Mo/Au interface, i.e., moving in the opposite direction (from Mo to Au) can be described by the AMM model. If this is the correct picture then the expression (21) can be rewritten as

$$\eta_{\text{eff}} = \eta_{\text{Au/Mo}} \frac{\eta_{s,\text{Au/Mo}}/\eta_{\text{Au/Mo}}}{1 + \eta_{\text{Mo/Au}}/\eta_{\text{esc,Mo/Si}}} = \nu \eta_{\text{Au/Mo}}, \qquad (23)$$

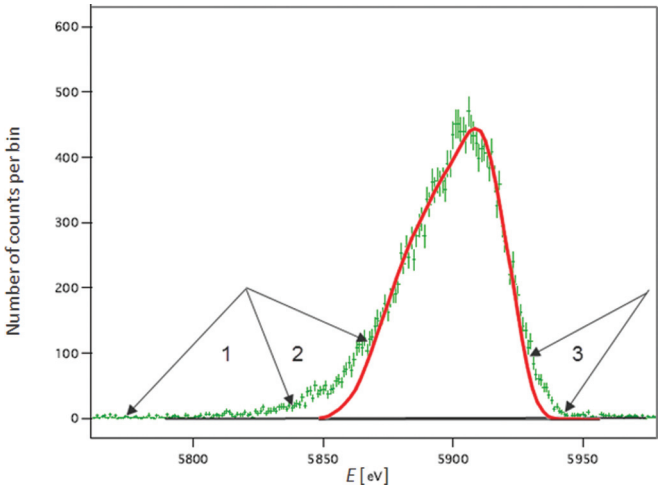

FIG. 10. (Color online) Comparison of simulation with experiment. Averaging the pulse in Fig. 9 over lateral coordinates with $\sigma_\eta = 0.065\bar{\eta}_{\text{eff}}$.

where $\eta_{s,\text{Au/Mo}}$ is the scattering-assisted transmission coefficient for high-frequency phonons from Au into Mo, while $\eta_{\text{Au/Mo}}$, $\eta_{\text{Mo/Au}}$, and $\eta_{\text{Mo/Si}}$ are AMM transmission coefficients, and ν is the fitting parameter. The scattering-assisted effective transmission coefficient, $\eta_{s,\text{Au/Mo}}$, differs from its AMM counterpart. Correspondingly, ν is likely to be less than 1 because of the large value of the ratio $\eta_{\text{Mo/Au}}/\eta_{\text{esc,Mo/Si}}$ being balanced by the factor $\frac{\eta_{s,\text{Au/Mo}}}{\eta_{\text{Au/Mo}}} \geqslant 1$. In our simulation of the lineshape in Figs. 8 and 9 we chose $\nu = 1/2$. The coupling constant entering the scattering cross sections may be large due to strong variation of material densities at the interface.

An important aspect of scattering-assisted phonon transfer is the statistical variation in the probability of scattering and the dependence of the scattering cross section of short-wavelength phonons on the local characteristics of the roughness of the interface. This introduces statistical fluctuations in the interface scattering and hence in the transmission coefficient in longitudinal directions. Thus, we may expect the effective transmission coefficient to be a random function of the lateral coordinate $\mathbf{r}$, $\eta_{\text{eff}}(\mathbf{r})$. We have implemented the averaging over the plane of the interface assuming a Gaussian distribution of η_{eff} with the variance σ_η about the mean value $\bar{\eta}_{\text{eff}}$, $P_\eta = \frac{1}{\sqrt{2}\sigma_\eta} \exp[-(\eta_{\text{eff}} - \bar{\eta}_{\text{eff}})^2/(2\sigma_\eta^2)]$. Figure 10 shows the result of this simulation. Overall, the agreement between the model and data looks much better. The slopes of the leading and trailing edges of the distribution are reproduced well with some tailing in the data still remaining on both sides.

Some of the remaining tailing can be explained by the model not having taken into account that 6.9% of x-ray absorptions generate phonons in the molybdenum part of the Mo/Au bilayer. The enhanced loss from Mo can result in a small separate peak on the left side of the spectrum. We could implement this by attributing some extra energy loss for all absorption events in the layer closest to the Si interface. In Fig. 8 these events are from the notional sublayer on the left. By including some small extra energy loss for

absorption in this sublayer, the corresponding spectrum is shifted further to the left, potentially giving a better fit to the data.

The broadening seen in the leading edge of the data in region 3 can be due to the fact that effective transmission has both coherent and scattering mediated regions. The presence of disorder-free patches of the interface, where this region is a small fraction of the total interface area, will mean that $\eta_{\rm eff}$ is locally suppressed and will result in smaller energy loss. Some of the remaining tailing in region 1 is difficult to explain within the phonon-loss model and probably has a different origin.

The extended tail in region 1 can be interpreted as being due to a universal mechanism related to loss of energy during the $E_0 \rightarrow E_1$ cascade. A certain percentage of the photon energy can leak via the loss of energetic electrons if their energy is larger than the work function from a metal by the time they hit the vacuum surface or dielectric interface. Our modeling of this mechanism of loss will be published in separate presentation.

Finally, the simulation based on the effective-medium model yields very similar results using same parameters as in Table I except taking for the mean sound velocity $c = 2.0 \times 10^5$ cm/s. This value is close to the weighted value for the Au/Mo bilayer accounting for fractional volumes of Au and Mo.

A. Energy loss and *e-e* interaction

So far we have not included in the modeling of the spectral lineshape the coordinate-independent term $E_{\rm loss,\Omega_D\rightarrow\Omega_1}$. Incorporation of this term results in shifting the pulse towards lower channels without changing its shape. The only extra fitting parameter entering this term as discussed in Sec. III is the threshold Ω_1. Including small energy loss, $E_{\rm loss,thermal}$, due to the additional thermal conductance of heat out of the microcalorimeter due to the MPT film being at a higher temperature for a short duration as discussed in the experimental section, we obtain for the total energy loss $E_{\rm loss} = E_{\rm loss,thermal} + E_{\rm loss,1} + E_{\rm loss,\Omega_D\rightarrow\Omega_1}$. For the set of parameters in Table I the averaged loss due to phonons of the first generation is $E_{\rm loss,1} = 0.7\%$. Taking $E_{\rm loss,thermal} = 0.4\%$ as estimated above we obtain that, in order to fit the experimental result of $E_{\rm loss} \approx 3.8\%$, the remaining loss term must account for 2.7% of the energy loss. Thus, as expected, this is the dominant loss term. Fitting this number yields the threshold Ω_1 by a factor 1.24 higher than given by expression (20), which is derived for the situation when $\tau_{e\text{-}e}(\Omega_1) \gg \tau_{\text{ph-}e}(\Omega_1)$. We therefore arrive at the conclusion that the electron-electron interaction in our Au film is relatively weak and only slightly modifies the lower threshold of the phonon stage of the down-conversion cascade.

This result further proves the consistency of our model. Indeed, at higher threshold E_1 the estimated electron-electron relaxation time was $\tau_{e\text{-}e}(E_1) \simeq 65$ fs. We have shown in Sec. III that the electron-electron interaction rate scales from this energy down practically to the Ω_1 threshold according to the $\epsilon^{3/2}$ law. Accounting the correction of 1.24 determined from fitting the energy loss to experiment we estimate the ratio $E_1/\Omega_1 \simeq 675$. Thus, the *e-e* interaction time scaled down to energy Ω_1 is estimated to be $\tau_{e\text{-}e}(\Omega_1) \simeq 1.1$ ns, which is close to our initial estimate $\tau_{\text{ph-}e}(\Omega_1) \simeq 1.5$ ns. The latter estimate was obtained by taking $\tau_{\text{ph-}e}(\Omega_{\rm D}) = 80$ ps from Table I and scaling its rate to the threshold Ω_1 according to the linear law (18).

One of the important practical implications of this result is that the *e-e* interaction in 330-nm-thick Au film has been found to be relatively weak, allowing therefore for an extended long-lasting phonon stage of down-conversion cascade. It is this property of the high-quality Au film of the Mo/Au bilayer that made possible the observation and identification of athermal phonon loss.

VI. DISCUSSION

Strong energy leaking from a thin film was experimentally observed by Cabrera[40] in a thin-film tungsten TES designed for detection of single optical photons. The measured fraction of energy detected with a W TES was surprisingly low at ~42%. This was attributed to the loss of athermal phonons. Such a big energy loss and reduction in energy efficiency is well known for detectors operating in the nonequilibrium regime; for example, STJs and MKIDs. These sensors operate at low temperatures $T \ll T_c$. Generation of non-pair-breaking phonons during the down-conversion cascade in a superconductor with finite gap Δ results in approximately 42% energy loss due to the decoupling of non-pair-breaking phonons from the condensate and the very weak interaction with quasiparticles. In a TES which is operated close to the critical temperature $T - T_c \ll T_c$, the order parameter $\Delta \rightarrow 0$ and all the nonequilibrium phonons generated can be reabsorbed by quasiparticles. This situation is very similar to the electron-phonon interaction in normal metals.

We are able to explain this high loss of energy using the same calculations used to explain the 3.4% energy loss from the escape of athermal phonons in our Mo/Au MPT bilayer. On this basis, we suggest that the large energy loss from a W TES can be explained by athermal phonon loss when taking into account all possible modes of athermal phonon loss. In an earlier analysis of spectral degradation of optical TESs due to phonon down-conversion noise,[4] the energy efficiency in a W TES described by Cabrera *et al.* was estimated to be 7%. However, this calculation only took into account the first two phonon generations. It is now clear that a dominant contribution to energy loss can be due to lower-energy phonons which are emitted during the extended $\Omega_{\rm D} \rightarrow \Omega_1$ stage.

Using the calculated Eliashberg function for tungsten[41] and parameters from Table II, and after averaging over the coordinates of absorption sites, we obtain from Eqs. (5), (7), (9), and (10) $E_{\rm loss} \simeq 46.9\%$. The breakdown of the observed losses due to different mechanisms for this experiment requires a special analysis. However, the overall number that we have calculated clearly dominates the observed 58% loss. It is also consistent with the magnitude of the experimentally observed improvement of energy efficiency from ~42% to ~80% that

TABLE II. Model parameters for W film.

τ_s ps	$\tau_{\text{ph-}e}(\Omega_{\rm D})$ ps	$c \times 10^5$ cm/s	$\eta_{\rm eff}$	D cm^2/s	t_{dc} ps
0.0125	13.3	3.18	0.043	35	0.40

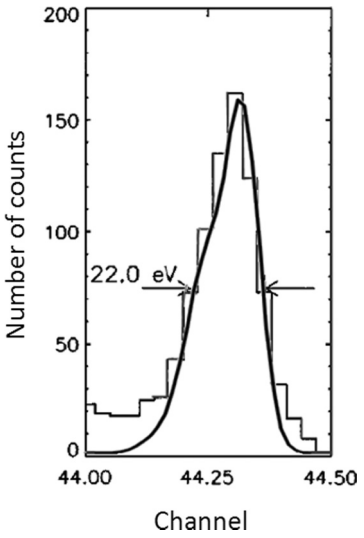

FIG. 11. This graph shows the spectrum of Mn K α observed by Verhoeve *et al.*[43] The solid line superimposed on this spectrum is the result of our simulated lineshape which takes into account the spatial broadening of the Mn K α complex due to loss of athermal phonons as well as intrinsic and electronic noise sources.

was seen in TESs that were fabricated on micromachined Si_3N_4 membranes,[1] which reduced the athermal phonon loss. The scattering rates derived from the parameters shown in Table II are consistent with the estimates of electron-phonon, phonon-electron, and electron-electron scattering rates in tungsten.[42] Both sets of data give close values for Ω_1 and $\tau_{e\text{-ph}}(\Omega_1) \ll \tau_{e\text{-}e}(\Omega_1)$ justifying our estimate energy loss.

It is remarkable that a relatively simple model can correctly describe the loss of athermal phonons in the process of energy deposition from such different thin metal films, even when the resulting fractional energy loss efficiency varies by over an order of magnitude.

In an experiment using an STJ consisting of Ta(110 nm)/Al(5 nm)/AlO_x/Al(5 nm)/Ta(95 nm) grown on a sapphire substrate by Verhoeve *etal.*,[43] the best spectral resolution achieved was $\Delta E = 15.7$ eV (FWHM) at 6 keV. Based on the responsivity of the STJ and the total noise from all noise contributions, the best achievable energy resolution was 8.9 eV (FWHM).

In Fig. 11 we show the results of spectral shape modeling for the geometry of this STJ. The material parameters for Ta used for this modeling are shown in Table III. Just as we did for the previous experiments, the intrinsic lineshape of Mn K α x-rays from Holzer was used,[39] and a detector resolution of 8.9 eV (FWHM) was assumed. In order to evaluate τ_s we used the calculated Eliashberg function and its first reciprocal moment λ for Ta.[34] The results from this modeling is shown in Fig. 11, as well as the original spectrum. It is apparent that the coordinate-dependent energy loss via escape of athermal phonons can adequately explain most of the measured spectrum.

TABLE III. Model parameters for Ta film.

τ_s ps	$\tau_{ph\text{-}e}(\Omega_D)$ ps	$c \times 10^5$ cm/s	σ eV	D cm^2/s	t_{dc} ps
0.026	1.2	2.33	3.8	500	0.25

In another similar experiment using a Ta-based x-ray absorber on a solid substrate, utilizing a distributed STJ detector readout, Li *et al.*[44] reported a spectral resolution of 12 eV (FWHM) for 6 keV x-rays, close to the theoretically achievable limit for this particular device. According to our models, the expected broadening that occurs due to the z-dependent athermal phonon energy loss for this 600-nm-thick Ta absorber is ~6 eV (FWHM). Therefore, this level of spectral broadening would not significantly impact the performance of this sensor.

VII. CONCLUSIONS

We have shown experimentally that, following a photon absorption in a thin metal film grown on a solid substrate, a substantial fraction of the energy deposited may be lost prior to establishing thermal equilibration due to the escape of athermal phonons to the substrate below. This form of energy loss can significantly affect the performance of high-resolution spectrometers on solid substrates. When the whole energy of the x-ray was retained in the spectrometer following its absorption in the absorber, the measured spectral resolution of the Mn K α complex was 4.3 eV (FWHM). However, for absorption events directly in the sensor film with a measured energy loss of 3.4%, the energy resolution deteriorated to ≈40 eV (FWHM). The main source of degradation in the soft-x-ray region is now understood to be due to the "z"-dependent energy of athermal phonon loss, while the effect of fluctuations in energy loss is small.

We have developed a theoretical model for simulation of the spectral lineshape and have shown that the latter is sensitive to details of energy deposition, energy exchange between electron and phonon systems, and phonon transmission to the substrate across the escape interface. Apart from trivial geometrical factors the amount of energy loss reflects the relative strength of electron-electron versus electron-phonon interactions over a broad spectral range (~1 eV) about the Fermi energy and the magnitude of the phonon transmission coefficient. The spectral lineshape is mostly determined by the high-energy, short (atomic scale) wavelength of first-generation phonons which are released during the initial stages of the energy down-conversion process. The loss of lower-energy athermal phonons of subsequent generations results only in a parallel shift of the spectral line without affecting its shape. Fitting the theoretical lineshape to the experimental lineshape allows us to evaluate the degree of scattering-assisted phonon transmission due to sub-nanometer-scale roughness of the interface.

Our relatively simple model explains a wide variety of measured energy losses and effects on measured spectral resolution. It is important for the design of future detectors with small or large regions of solid substrate contact.

ACKNOWLEDGMENTS

The authors would like to acknowledge useful discussion with Blas Cabrera, Aaron Miller, and Megan Eckart.

[1] A. E. Lita, A. J. Miller, and S. Nam, J. Low Temp. Phys. **151**, 125 (2008)

[2] A. G. Kozorezov, A. F. Volkov, J. K. Wigmore, A. Peacock, A. Poelaert, and R. den Hartog, Phys. Rev. B **61**, 11807 (2000).

[3] D. D. E. Martin, P. Verhoeve, A. Peacock, A. G. Kozorezov, J. K. Wigmore, H. Rogalla, and R. Venn, Appl. Phys. Lett. **88**, 123510 (2006).

[4] A. G. Kozorezov, J. K. Wigmore, D. Martin, P. Verhoeve, and A. Peacock, Appl. Phys. Lett. **89**, 223510 (2006).

[5] H. F. C. Hoevers *et al.*, Appl. Phys. Lett. **86**, 251903 (2005).

[6] C. K. Stahle *et al.*, Nucl. Instrum. Methods Phys. Res., Sect. A **520**, 466 (2004).

[7] S. R. Bandler, A.-D. Brown, J. Chervenak, E. Figueroa-Feliciano, F. Finkbeiner, N. Iyomoto, R. L. Kelley, C. Kilbourne, F. S. Porter, and S. J. Smith, J. Low Temp. Phys. **151**, 400 (2008).

[8] M. K. Bacrania, A. S. Hoover, P. J. Karpius, M. W. Rabin, C. R. Rudy, D. T. Vo, J. A. Beall, D. A. Bennett, W. B. Doriese, G. C. Hilton, R. D. Horansky, K. D. Irwin, N. Jethava, E. Sassi, J. N. Ullom, and L. R. Vale, IEEE Trans. Nucl. Sci. **56**, 2299 (2009).

[9] S. R. Bandler *et al.*, Proc. SPIE **7021**, 70211K (2008).

[10] S. J. Smith, J. S. Adams, C. N. Bailey, S. R. Bandler, J. A. Chervenak, M. E. Eckart, F. M. Finkbeiner, R. L. Kelley, C. A. Kilbourne, F. S. Porter, and J. E. Sadleir, J. Low Temp. Phys. **167**, 168 (2012).

[11] S. R. Bandler, K. D. Irwin, D. Kelly, P. N. Nagler, J.-P. Porst, H. Rotzinger, J. E. Sadleir, G. M. Seidel, S. J. Smith, and T. R. Stevenson, J. Low Temp. Phys. **167**, 254 (2012).

[12] K. D. Irwin and G. C. Hilton, in *Cryogenic Particle Detection*, Topics in Applied Physics Vol. 99, edited by C. Enss (Springer, Heidelberg, 2005), pp. 63–152.

[13] A. Fleischmann, C. Enss, and G. M. Seidel, in *Cryogenic Particle Detection*, Topics in Applied Physics Vol. 99, edited by C. Enss (Springer, Heidelberg, 2005), pp. 151–216.

[14] P. C. Nagler, J. S. Adams, M. A. Balvin, S. R. Bandler, K. L. Denis, W.-T. Hsieh, D. P. Kelly, J.-P. Porst, J. E. Sadleir, G. M. Seidel, S. J. Smith, and T. R. Stevenson, J. Low Temp. Phys. **167**, 455 (2012).

[15] T. R. Stevenson *et al.*, IEEE Trans. Appl. Supercond. (accepted for publication).

[16] H. Rotzinger *et al.*, J. Low Temp. Phys. **151**, 351 (2008).

[17] A. Lita *et al.*, J. Low Temp. Phys. **151**, 125 (2009).

[18] W.-T. Hsieh, J. S. Adams, S. R. Bandler, J. Beyer, K. Denis, H. Eguchi, H. Rotzinger, G. Schneider, G. M. Seidel, T. R. Stevenson, and D. Travers, J. Low Temp. Phys. **151**, 357 (2008).

[19] D. Drung *et al.*, IEEE Trans. Appl. Supercond. **17**, 699 (2007).

[20] A. G. Kozorezov, J. K. Wigmore, D. Martin, P. Verhoeve, and A. Peacock, Phys. Rev. B **75**, 094513 (2007).

[21] A. G. Kozorezov, J. K. Wigmore, D. Martin, P. Verhoeve, and A. Peacock, J. Low Temp. Phys. **151**, 51 (2008).

[22] D. Martin *et al.*, Nucl. Instrum. Methods Phys. Res., Sect. A **370**, 88 (1996).

[23] H. Pressler, M. Ohkubo, M. Koike, T. Zama, T. Nakamura, and M. Katagiri, Appl. Phys. Lett. **77**, 4055 (2000).

[24] Roland den Hartog, A. G. Kozorezov, J. K. Wigmore, D. Martin, P. Verhoeve, A. Peacock, A. Poelaert, and G. Brammertz, Phys. Rev. B **66**, 094511 (2002).

[25] O. J. Luiten, M. L. van den Berg, J. Gomez Rivas, M. P. Bruijn, F. B. Kiewiet, and P. A. J. de Korte, *Proceedings of the Seventh International Workshop on Low Temperature Detectors (LTD-7)*, edited by S. Cooper (Munich, 1997), p. 25.

[26] R. Christiano *et al.*, J. Appl. Phys. **86**, 4580 (1999).

[27] L. Parlato *et al.*, Nucl. Instrum. Methods Phys. Res., Sect. A **440**, 15 (2000).

[28] A. G. Kozorezov, J. K. Wigmore, R. den Hartog, D. Martin, P. Verhoeve, and A. Peacock, Phys. Rev. B **66**, 094510 (2002).

[29] B. I. Altshuler and A. G. Aronov, in *Electron-Electron Interactions in Disordered Systems*, edited by A. L. Efros and M. Pollak (Amsterdam, North-Holland, 1985).

[30] M. Kaveh and N. Wiser, Adv. Phys. **33**, 257 (1984).

[31] R. A. Ferrell, Phys. Rev. **101**, 554 (1956).

[32] A. G. Kozorezov, J. Low Temp. Phys. **167**, 473 (2012).

[33] A. G. M. Jansen, F. M. Mueller, and P. Wyder, Phys. Rev. B **16**, 1325 (1977).

[34] S. Y. Savrasov and D. Y. Savrasov, Phys. Rev. B **54**, 16487 (1996).

[35] S. B. Kaplan, J. Low Temp. Phys. **37**, 343 (1979).

[36] E. T. Swartz and R. O. Pohl, Rev. Mod. Phys. **61**, 605 (1989).

[37] A. G. Kozorezov, J. K. Wigmore, C. Erd, A. Peacock, and A. Poelaert, Phys. Rev. B **57**, 7411 (1998).

[38] G. Fagas, A. G. Kozorezov, C. J. Lambert, J. K. Wigmore, A. Peacock, A. Poelaert, and R. den Hartog, Phys. Rev. B **60**, 6459 (1999).

[39] G. Holzer, M. Fritsch, M. Deutsch, J. Hartwig, and E. Forster, Phys. Rev. A **56**, 4554 (1997).

[40] B. Cabrera, R. M. Clarke, P. Colling, A. J. Miller, S. Nam, and R. W. Romani, Appl. Phys. Lett. **73**, 735 (1998).

[41] Asier Eiguren, Claudia Ambrosch-Draxl, and Pedro M. Echenique, Phys. Rev. B **79**, 245103 (2009).

[42] B. Cabrera, Nucl. Instrum. Methods Phys. Res., Sect. A **370**, 150 (1996).

[43] P. Verhoeve, N. Rando, A. Peacock, A. van Dordrecht, B. G. Taylor, and D. J. Goldie, Appl. Phys. Lett. **72**, 3359 (1998).

[44] L. Li, L. Frunzio, C. Wilson, D. E. Prober, A. E. Szymkowiak, and S. H. Moseley, J. Appl. Phys. **90**, 3645 (2001).